Carbon 182 (2021) 223–232

Contents lists available at ScienceDirect

Carbon

journal homepage: www.elsevier.com/locate/carbon

Research Article

Geometric model of 3D curved graphene with chemical dopants

Andreas Dechant [a, 1], Tatsuhiko Ohto [b, 1], Yoshikazu Ito [c], Marina V. Makarova [d], Yusuke Kawabe [e], Tatsufumi Agari [e], Hikaru Kumai [e], Yasufumi Takahashi [d, e, f], Hisashi Naito [g], Motoko Kotani [a, h, *]

[a] WPI Advanced Institute for Materials Research, Tohoku University, Sendai, 980-8577, Japan
[b] Graduate School of Engineering Science, Osaka University, 1-3 Machikaneyama, Toyonaka, 560-8531, Japan
[c] Institute of Applied Physics, Graduate School of Pure and Applied Sciences, University of Tsukuba, Tsukuba, 305-8573, Japan
[d] WPI Nano Life Science Institute (NanoLSI, WPI), Kanazawa University, Kakuma-machi, Kanazawa, Ishikawa 920-1192, Japan
[e] Division of Electrical Engineering and Computer Science, Kanazawa University, Kanazawa, 920-1192, Japan
[f] Precursory Research for Embryonic Science and Technology (PRESTO), Japan Science and Technology Agency (JST), Saitama, 332-0012, Japan
[g] Graduate School of Mathematics, Nagoya University, Nagoya, 464-8602, Japan
[h] Mathematical Institute, Graduate School of Science, Tohoku University, Sendai, 980-8578, Japan

ARTICLE INFO

Article history:
Received 22 February 2021
Received in revised form
28 May 2021
Accepted 1 June 2021
Available online 4 June 2021

Keywords:
Gauss curvatures
Catalytic properties
3D curved graphene
Mathematical modeling
Chemical doping
Carbon network

ABSTRACT

Geometric structures of carbon networks are key in designing their material properties. In particular, optimization of curved structures through the introduction of topological defects and doping of heteroatoms in the lattice is crucial to the design of carbon-based, non-noble-metal-free catalysts. A simple and practical mathematical model based on discrete geometric analysis is proposed to describe the geometric features of carbon networks and their relationships to their material properties. This model can pre-screen candidates for novel material design, and these candidates can be further examined by the density functional theory (DFT). Inspired by observations regarding the preferential doping of heteroatoms at local curved sites, the important characteristics of the candidate material were experimentally realized, and its enhanced catalytic activity facilitated by chemical dopants was confirmed in the designed carbon network.

1. Introduction

Following the discovery of carbon network materials that contain sp^2-hybridized C–C bonds, such as 2D graphene [1,2], similar materials with novel functions have been synthesized for promising applications in post-silicon devices [3–6], as well as energy devices, such as supercapacitors [7–10], batteries [11–14], and catalysts [15–21]. In particular, three-dimensional (3D) carbon networks and 2D-like carbon networks expanding in the 3D space such as 3D curved graphene, have become a fascinating research target owing to their unique physical properties that are typically not exhibited by carbon network materials without 3D structures [22–25]. These networks are constructed from local (atomic-scale) curvatures induced by topological defects or heteroatom doping in the lattices and mesoscopic bending of graphene sheets. Previous reports have suggested that the unique physical properties of 3D curved graphene can be attributed to their geometric features. However, the origin of 3D carbon networks that exhibit better performances than 2D carbon networks has not been comprehensively understood because of gaps that exist between theoretical simulations using force field (FF) or density functional theory (DFT), and experiments.

The fine control of structures, such as the catalytic reaction field, and the stability of 3D network structures is important in catalyst design [25,26]. To realize a decent design of the catalytic reaction field, nanometer-sized models are typically constructed owing to the limitation of computational resources. This strongly restricts the interpretation/prediction of their global properties and hinders complete understanding of the influence of local properties on global properties. Moreover, interpreting the origin of instability in the entire 3D carbon network using these limited models is

* Corresponding author. WPI Advanced Institute for Materials Research, Tohoku University, Sendai, 980-8577, Japan.
E-mail address: motoko.kotani.d3@tohoku.ac.jp (M. Kotani).
[1] These authors contributed equally to this work.

https://doi.org/10.1016/j.carbon.2021.06.004

challenging. Therefore, two different types of curvatures have been introduced as fundamental mathematical concepts in discrete surface theory to resolve these issues [27]; one involves the Gauss curvature [27]. When five hexagons and a pentagon (heptagon) share an atom, the plane near the atom becomes convex-shaped (saddle-shaped). In such a situation, the Gauss curvature at the atom is positive (negative). Importantly, regions near the five-membered (seven-membered) ring are influenced by certain frustrations attributed to their geometry (termed as "geometric frustrations") [28]. In other words, the Gauss curvature describes internal structural frustration and quantifies the geometry of the catalytic reaction field. The other aspect involves the mean curvature [27], which expresses the stability of the lattice by minimizing the energy of the geometric model. In other words, it describes structural stability under external deformation and quantifies the structural stability of the entire model. Based on these aspects, a mathematical model known as "standard realization," which provides a direct and intuitive understanding of the relationship between local structures and global properties, has been proposed to identify energetically stable structures of 3D curved graphene by utilizing these curvatures and to design stable and novel carbon network materials with desirable properties.

The mathematical model of standard realization saves substantial computational resources, which are typically required by DFT in pre-screening potential materials; its accuracy is qualitatively similar to that of DFT. Although the standard realization captures the universal and essential features of certain physical systems [28,29], the models and their subsequent analysis cannot be applied to a doped graphene system where a single carbon atom in the lattice in the form of catalytic reaction fields is replaced by a single heteroatom, owing to oversimplification of physical systems. To refine the standard realization, repulsive next-nearest-neighbor (NNN) interactions have been introduced in the present study to expand it for universal use with respect to the minimum requirements of the physical system (Fig. 1A). The improved model is denoted as "*standard realization with repulsive interactions*" (SRRI). In particular, the catalytic properties of 3D curved graphene with chemical dopants can be a simple target to investigate the possibilities of this mathematical tool for pre-screening and designing novel materials.

In this study, the important and minimum characteristics of physical systems were extracted using SRRI to investigate the influence of the change in geometric features on physical properties, and to evaluate the accuracy outputted from the mathematical model for pre-screening the catalyst designs. A mathematical model of 3D curved graphene with topological defects was designed; it was subsequently validated, and its accuracy cross-checked with DFT calculations. The geometric frustration energy, which is locally controlled by the chemical dopants incorporated into the lattice, enables the geometric analysis of the catalytic reaction field (i.e., chemical doping sites), where substantial changes occur in the Gauss curvature based on the lattice configurations. Finally, the catalytic activity of 3D curved graphene with chemical dopants, as suggested by the pre-screening output of the models, was experimentally investigated by on-site electrochemical measurements with scanning electrochemical cell microscopy (SECCM) [30–35] to link the geometry (local structures) and catalytic properties (global properties). This sequential approach using simple mathematical modeling over atomistic calculations for experimental realization provides not only a good interpretation of material properties but also an effective pathway to save computational resources and to guide the design of new materials via their geometry.

2. Materials and methods

2.1. Standard realization and DFT calculations

Structural optimization of non-doped and nitrogen-doped graphene containing 5–7 defects was performed either by SRRI or DFT. A periodic boundary condition was applied, and the graphene unit cell contained 230 atoms. For the SRRI model, the energy and force were calculated using Eq. (1). In the case of graphitic nitrogen, because the interactions were based on electrostatic repulsion, κ_{ij} were assumed to be unchanged to leading order. On the other hand, the spring constants k_{ij} of the NN of the nitrogen atom were increased by a factor of 1.2, which corresponded to the difference in the electronegativity of carbon and nitrogen. DFT calculations were performed using the Vienna *ab initio* simulation package (VASP) [36], based on the spin-polarized density functional theory within the generalized gradient approximation (GGA). The electron–ion interactions were described by frozen core, all-electron projector augmented-wave pseudopotentials [37]; the GGA exchange-correlation potential was also adopted in the form of the Perdew–Burke–Ernzerhof (PBE) [38] function. The electron wave-functions were expanded using a plane-wave basis set with a cut-off energy of 400.0 eV. All calculations were performed by sampling the Brillouin zone at the gamma point only. In the structure relaxations, the atomic geometries were fully optimized until the Hellmann–Feynman forces were less than 0.01 eV/Å. Further details and relevant references are presented in the supplementary text.

2.2. Material fabrication

NiO nanoparticles [39] (~10 nm) drop-casted on Cu sheets were annealed at 350 °C for 25 min and continuously annealed at 750 °C for 3 min to clean the Ni surface under a mixed atmosphere of H_2 (100 sccm) and Ar (200 sccm). Subsequently, graphene/chemically doped graphene was grown at 800 °C under a mixed atmosphere of H_2 (100 sccm), Ar (200 sccm), benzene (0.1 mbar, 99.8%, anhydrous), pyridine (0.1 mbar, 99.8%, anhydrous), and/or thiophene (0.2 mbar, 99%, anhydrous). The furnace was quickly opened, and the inner quartz tube was cooled with a fan to room temperature. The Ni substrates were dissolved in a 0.2 M $Fe(NO_3)_3$ solution for two days and in a 1.0 M HCl solution for 3 days of etching at 50 °C. The resulting graphene sheets from the solution were repeatedly rinsed with pure water five times and kept on water for 3 days.

2.3. Imaging and spectroscopic characterization

The microstructures of chemically doped and curved graphenes were characterized by scanning electron microscopy (SEM, JEOL JSM-6700) and transmission electron microscopy (JEM-ARM200F) with electron energy-loss spectroscopy (EELS; GATAN Enfinium). The samples were transferred on a Cu grid without a carbon support film.

2.4. Electrochemical characterization

The SECCM employed a moveable nanopipette probe containing a 0.5 M H_2SO_4 solution and a Pd–H_2 quasi-reference counter electrode (QRCE). The nanopipette was prepared by pulling a borosilicate glass capillary (GC150F-10 from Harvard Apparatus). The nanopipette diameter was ~100 nm. In the case of chloride-ion-free solutions, Pd–H_2 QRCE was generally used for SECCM experiments [40,41]. All the potentials were converted into electric potentials

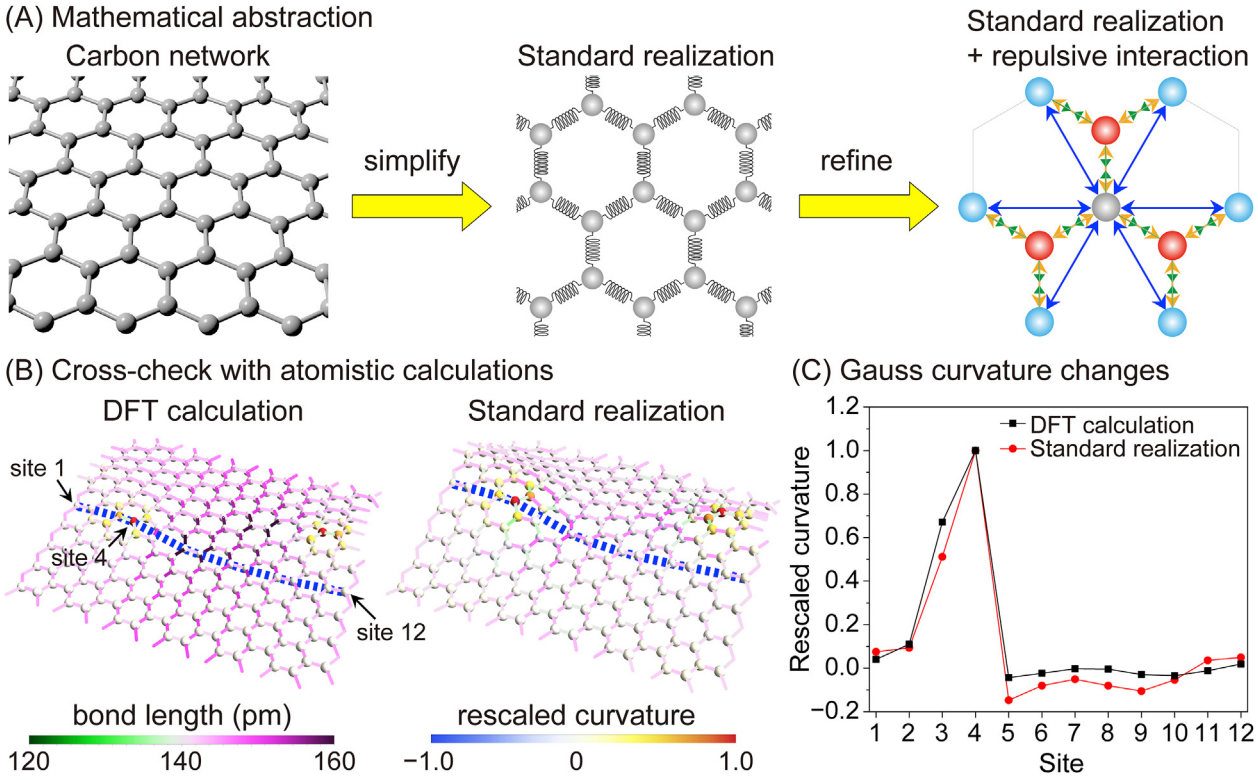

Fig. 1. Simplification of carbon network and mathematical determination of geometry. (A) Mathematical abstraction from carbon network to mathematical modeling for the standard realization and the standard realization with repulsive interaction. The stability of external deformations of the surfaces is described by the mean curvature in classical geometry. Using its discrete analog [29], the stable configuration of a carbon network can be realized by the simple "standard realization" mathematical model. The modification of this model considers repulsive forces between atoms, as shown in the present study, and is denoted as "standard realization with repulsive interactions." Red and bright blue balls represent nearest-neighbor and NNN atoms from the central gray atom, respectively. Green arrows show attractive linear forces, whereas blue and orange arrows show repulsive Coulomb forces. (B) Construction of geometric structures by SRRI and by DFT as a cross-check for a periodic lattice with two 5–7 defects per unit cell. Changes in bond length and Gauss curvatures are shown by colored cylinders and colored vertices (spheres), respectively. Longer (purple) or shorter (green) bonds are relative to defect-free graphene, and the colors of the vertices are normalized by their respective maximum value. (C) Site dependence of the Gauss curvature changes along the path through the lattice marked with blue dotted lines shown in Fig. 1B. (A colour version of this figure can be viewed online.)

when the reversible hydrogen electrode was used as the reference electrode. The scanning protocol details are described in the Supplementary Information.

3. Results

3.1. Mathematical modeling by standard realization with repulsive interactions

The standard realization of a crystal lattice provides the most symmetric configuration of a given graph structure (lattice of bonds between atoms) using normalization for primitive cells to have a constant volume, and is defined by the unique (up to translations and scaling) minimizer of the energy $\sum_{i,j\in \mathrm{NN}} \frac{k_{ij}}{2}\|x_i - x_j\|^2$, where x_i is the position of the i-th atom and k_{ij} are defined by the adjacency matrix of the weighted graph; k_{ij} physically represent spring constants. In other words, the standard realization is a mathematical model of the crystal lattice as an elastic network (Fig. 1A), whose NN atoms are connected by springs with periodic boundary conditions. The standard realization behaves as a minimizer of energy as a consequence of the symmetry of the structures described by harmonic oscillation models and reproduces classical crystal structures such as those of the sp^2-carbon network (i.e., graphene) [29]. However, because the interactive forces are purely attractive, the standard realization of a lattice with two-dimensional periodicity is always flat.

Because of this crucial difference between the lattice obtained by the standard realization without repulsive interaction and the benchmark lattice obtained by DFT calculations, a model with repulsive forces is introduced:

$$U = \sum_{i,j\in \mathrm{NN}} \frac{k_{ij}}{2}\|x_i - x_j\|^2 + \sum_{i,j\in \mathrm{NNN}} \frac{\kappa_{ij} d^3}{\|x_i - x_j\|}, \tag{1}$$

where U is the total energy. The second term in Eq. (1) is a model of repulsive interactions between NNN, where κ_{ij} describe their strength of bonding and d is the length scale. Accordingly, SRRI is a simple model with the first term in Eq. (1) representing attractive interactions between NN atoms by covalent bonds and the second term in Eq. (1) representing repulsive interactions by electrostatic repulsion between the ion cores in NNN atoms (Figs. S1 and S2 and supplementary text). In the case of the graphene lattice, because all the atoms are equivalent, k_{ij} and κ_{ij} were simplified as $k_{ij}\equiv k$ and $\kappa_{ij}\equiv\kappa$. The parameter κ was further uniquely determined by forcing a stable minimum of the potential with a honeycomb lattice with lattice constant $d = 1.42$ Å. This led to $\kappa = \frac{\sqrt{3}}{2}k$ and $k = 11.6$ eV/Å^2 (Figs. S1 and S2 and supplementary text). Thus, the model with repulsive interactions simplifies physical interactions and yields a curved graphene lattice even for two-dimensional models with 5–7 defects.

For a given connectivity of the lattice, Eq. (1) provides a uniquely

curved equilibrium lattice with an overall length scale d, and also provides an optimal distribution of the mean curvature, because the mean curvature expresses stability with respect to interactions with the physical space (three-dimensional Euclidean space). Moreover, the presence of the length scale enables optimization of the lattice volume. Similar to the standard realization without repulsive interactions, SRRI in the curved graphene lattice also exhibits conceptual simplicity, a unique connectivity-structure relationship, and absence of free parameters. In addition, SRRI provides accurate suggestions for 3D curved graphene lattices with defects at a high computational speed. Concretely, single-point calculations of the lattice (Fig. 1B) consisting of 216 atoms per unit cell take ~39 μs on a personal desktop computer; this is more than 15 times faster than that of OPLS-AA [42], which is the simplest fixed-valence FF model (Tables S1 and S2), and requires considerably fewer model parameters (Table S2). Furthermore, SRRI can be applied to parallel computing systems (supplementary information). Such differences in speed and parameters allow SRRI, in principle, to analyze models with infinite sizes, and the resulting data and physical properties can be complemented with FF/DFT (Table S1 and supplementary information) and can also be compared with a global continuous model based on the continuous approximation theory [27,43].

3.2. Cross-check between standard realization and DFT calculations

SRRI was computed by minimizing the interaction potential in Eq. (1) for a periodic graphene lattice with two 5–7 defects per unit cell, as an example of a 3D curved graphene lattice with non-zero Gauss curvature. These results were compared to a benchmark lattice obtained using DFT calculations. Qualitatively, both lattices are very similar (Fig. 1B). For the C–C bond lengths, the agreement is qualitative with a relative deviation of bond length that is less than 19% between the two lattices. For the Gauss curvature, SRRI overestimates the curvature by a factor of ~3; however, the qualitative distribution of the Gauss curvature over the lattice is in very good agreement when rescaled by its maximum value (Fig. 1C). These geometric features are expected to be closely related to the geometrically frustrated energy, which is locally induced by the defects, as can be seen by comparing the geometry near the pentagon and heptagon rings.

The bond lengths near the pentagon (heptagon) tend to be shorter (longer) than those of the hexagons in the graphitic lattice, even in the SRRI case [27,28]. Such tendencies have been explained by mathematical arguments that depend on the eigenvalues of the graph Laplacian [44,45]. Therefore, the positivity of Gauss curvatures near the pentagon rings is relatively large, because the difference in normal vectors of the neighboring atoms is relatively large. By contrast, the negativity of Gauss curvatures near the heptagon rings is comparatively small because the difference in normal vectors of the neighboring atoms is relatively small. Moreover, in the case of SRRI, a shorter (longer) bond length yields a large (small) number of NNN repulsive interactions. This competition between incompatible tendencies (short NN distance and large NNN distance) results in the force that pushes atoms out-of-plane and yields a large degree of geometric frustrations.

A possible explanation for the larger curvature in SRRI is that the mathematical model neglects delocalization effects for simplification, particularly those of the π-electrons in the rings, which may favor more planar configurations. A similar comparison for a flat graphene lattice was carried out with one Thrower–Stone–Wales-type (TSW) defect per unit cell, as a second cross-check. A good agreement between the SRRI and the DFT calculations was observed again (the relative deviation of bond length was less than 4.1%, Fig. S3).

Considering the viewpoint of physics, DFT calculations indicate that the 5–7 defects induce a slightly heterogeneous charge distribution (Fig. S4). In particular, the pentagonal ring tends to be negatively charged, whereas the common edge of the pentagon–heptagon is positively charged. Moreover, the geometric frustrations introduced by the 5–7 defect enhance the density of states at the Fermi level compared to that of pristine graphene (Fig. S5). Several DFT calculations have reported on this defect-induced enhancement of density of states [46,47]. This suggests that the five-membered-ring side featuring a high Gauss curvature can increase the density of states. Several studies have described the relationship between the geometric structure and electronic properties [48,49]. Further systematic analysis and mathematical considerations on these aspects in a more general setting could provide new insight into the connection of discrete surfaces and physical properties.

3.3. Suggestion of available doping sites in a flat lattice

The influence of the changes in Gauss curvatures of the catalytic reaction field induced by topological defects and a single heteroatom, such as graphitic nitrogen (a nitrogen atom bonded to three neighboring carbon atoms), incorporated into the flat graphene lattice, was examined (Fig. 2 and Fig. S6). In SRRI, a heteroatom differs from carbon only via the constants k_{ij} and κ_{ij} in Eq. (1) that describe its interaction with its neighbors. As a result, the C–N bonds are shorter than the C–C bonds in the same model, which agrees with the DFT calculations. Starting from the lattice with two 5–7 defects per unit cell shown in Fig. 1B, a selected carbon atom is replaced with a graphitic nitrogen atom, and the lattice is relaxed using SRRI and DFT calculations. This process is repeated for different doping positions, and the position dependence of bond length and Gauss curvature can be obtained (FIgs. S7–S9 and Table S3). Similar to the undoped case, good agreements (relative deviation of bond length less than 12% for doping near pentagon (Fig. 2(A and C)) and 26% for doping near heptagon (Fig. 2(B and D)) were seen between the doped lattices obtained by SRRI and DFT calculations. The positive Gauss curvature was found near the pentagon ring with the maximum curvature at site 13, whereas the lattice was flat near the heptagon ring at site 8 (solid symbols in Fig. 2 (E and F)). The positive curvature significantly decreases when the graphitic nitrogen is doped at site 14 near the pentagon ring (empty symbols in Fig. 2E). Conversely, when the graphitic nitrogen atom is doped next to site 8 in the heptagon ring, the negative curvature shows almost no changes (empty symbols in Fig. 2F). This behavior indicates that the highly positive curvature is relaxed by the dopant; this is consistent between SRRI (red symbols) and DFT calculations (black symbols).

The relationship between the curvature relaxation and doping energy (i.e., the total energy of the doped system relative to the most stable one) was investigated. Because the shorter C–C bond near the pentagons can be replaced by the short C–N bond, the curvature relaxation is expected to be preferable for doping graphitic nitrogen. Accordingly, a correlation between the normal vector that is tuned by bond lengths near the doping site and the doping availability of the nitrogen dopant is expected (Fig. 3A and Table S3). The average bond length of the pre-doping system is computed at each site in the SRRI model (red symbols) and DFT calculations (black symbols), and plotted against the doping

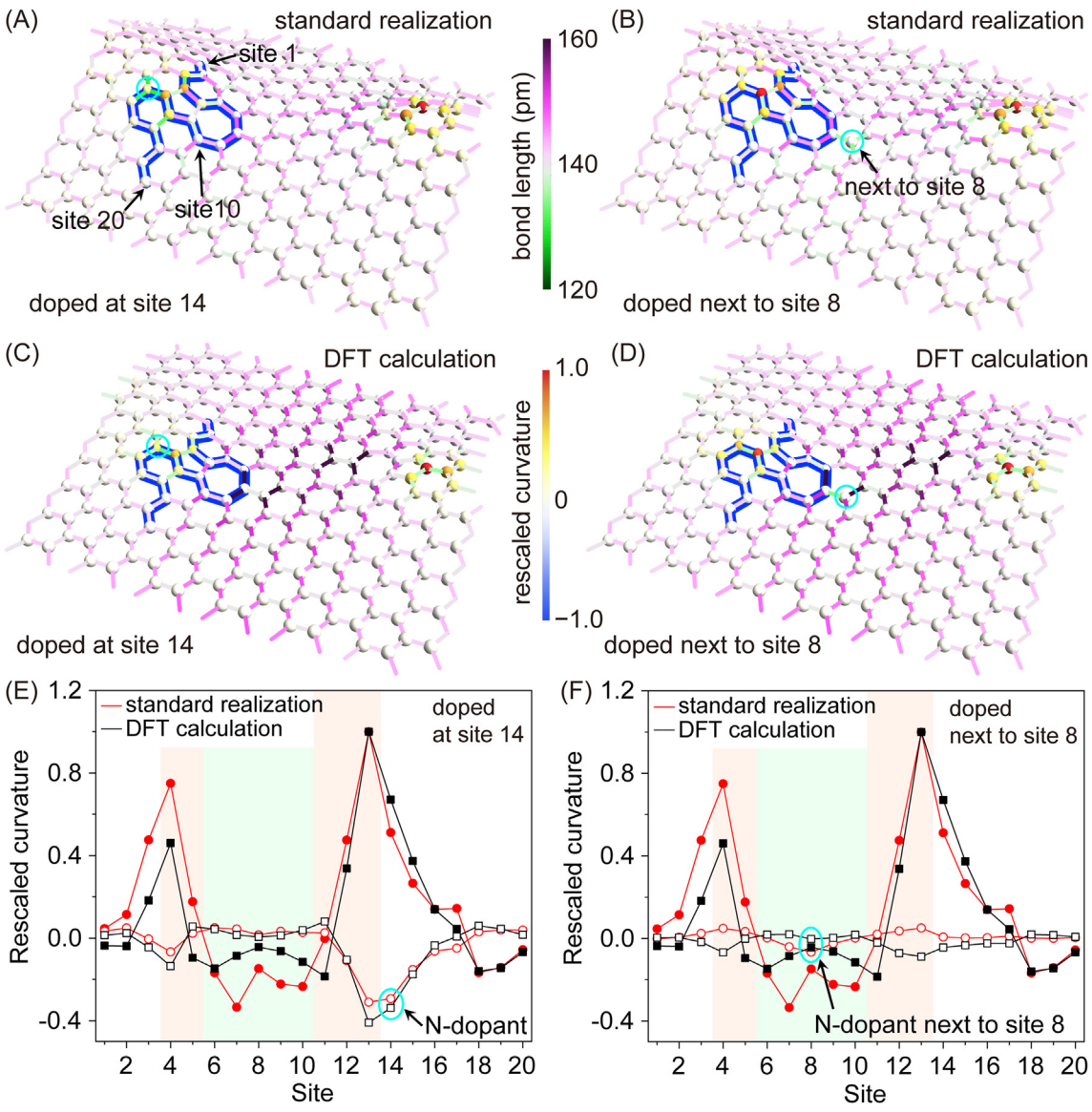

Fig. 2. Correlations between geometric features and doping availability for graphitic N. Doping of a single graphitic nitrogen atom into site 14 with an adjacent pentagon ring simulated by (A) SRRI and (C) DFT calculations. Doping of a single graphitic nitrogen atom into a position next to site 8 with an adjacent heptagon ring simulated by (B) SRRI and (D) DFT calculations. Numbers in (A) represent the site positions shown in (E and F). (E) Position dependence of the rescaled curvature near the pentagon ring along the blue line shown in (A and C). (F) Position dependence of the rescaled curvature near the heptagon ring along the blue line shown in (B and D). Blue lines in (A–D) represent guides for the sites employed in the rescaled curvature plots in (E) and (F). Filled symbols represent rescaled curvatures before doping and open symbols represent the difference between the rescaled curvatures after and before doping. Cyan circles represent the nitrogen position in the pentagon ring shown in (A and C) and the position next to nitrogen near the heptagon ring shown in (B and D). The red and green shaded regions represent the pentagon and heptagon sites in the blue line shown in (A and C), respectively. (A colour version of this figure can be viewed online.)

energies, which is set at 0 eV. An almost linear relation between the average bond length and the doping energy is observed, indicating that sites with shorter bonds are preferred as doping locations. SRRI shows a linear relationship because the energy is a function of only the distance between atoms. The large curvature changes (%), specifically the large positive Gauss curvature becoming nearly zero, are noted to correlate with lower doping energies (Fig. 3B and more details in Fig. 2 (E and F)). Because the Gauss curvature appears as a consequence of geometric frustration, the release of geometric frustration can stabilize the dopant. The direct correspondences between geometric features and doping energies facilitate the suggestion of the preferred doping sites using bond lengths and Gauss curvatures obtained from SRRI. A similar analysis was also performed for doping a single graphitic nitrogen atom into a lattice including a TSW defect (Fig. S5) and for doping a single pyridinic nitrogen atom (a nitrogen atom bonded to two neighboring carbon atoms) into the lattice shown in Fig. 1B (Figs. S10–S12 and supplementary text). In both cases, the preferred doping sites were found to be those with short bonds, corresponding to a relationship similar to the one depicted in Fig. 3; the Gauss curvature of the lattice was likewise reduced when the pyridinic nitrogen was doped near a pentagon with a vacancy defect (Figs. S10–S11). Furthermore, the doping accessibility of graphitic and pyridinic nitrogen in the lattice was compared. The doping of pyridinic nitrogen into the sites with large Gauss curvatures was energetically preferable owing to the concentrated doped pyridinic nitrogen near the defects. By contrast, the doped graphitic nitrogen was not concentrated near the defects owing to the small

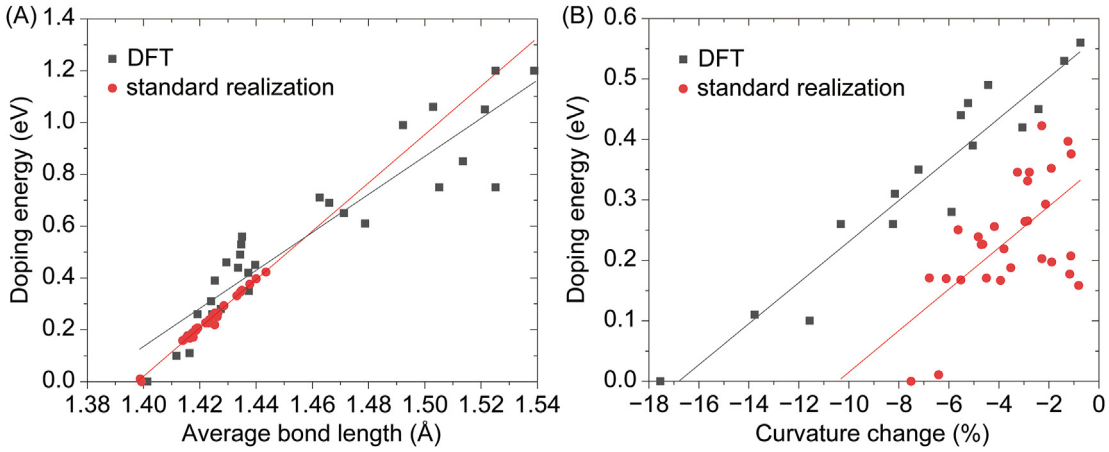

Fig. 3. Relation between bond length, curvatures, and doping energy for graphitic N. (A) Doping energy vs. bond length: the horizontal axis shows the average length of the three nearest neighboring bonds of the respective carbon atoms in the undoped system, and the vertical axis shows the relative total energy (eV) of the system with a doped graphitic nitrogen at that site. The energy of the most stable system is set to zero when graphitic nitrogen is doped to site 4, as shown in Fig. S7. (B) Doping energy vs. change in the Gauss curvatures: the horizontal axis represents the relative change in the Gauss curvatures (summed over all atoms of the unit cell in Fig. 1(B) after doping. In both (A) and (B), the lines represent a linear least-squares fit to the respective data. (A colour version of this figure can be viewed online.)

differences of doping energies at the site with high and low Gauss curvatures (Fig. S13).

3.4. Doping availability and suggestion of doping positions in a curved lattice

Two scenarios involving the generated defects exist: one involves defects generated on a flat graphene lattice, whereas the other involves defects generated on a curved graphene lattice with a low curvature for constructing the entire 3D network; the first scenario has been discussed in sections 3.1–3.3, wherein the defects were noted to influence the Gauss curvature in terms of the geometry of the catalytic reaction field. Subsequently, the second case was considered, in which the flat graphene lattice is bent with two 5–7 defects to form a curved lattice to examine the stability under external deformations (i.e., 30° bending, Fig. S14). As a result, the Gauss curvature of the bent lattice changes only slightly compared to that of the flat lattice, whereas its mean curvature significantly changes and strongly reflects the structural stability of the entire model (mathematical details have been provided in the Supplementary Information and Fig. S15). This indicates that the mesoscopic bending of a graphene sheet does not significantly affect the Gauss curvature. Therefore, the difference in doping availability of the mean curvature can be identified. The bent graphene shows a 0.06–0.20 eV lower doping energy of graphitic nitrogen as calculated by DFT (Table S4). Moreover, a large reduction in doping energy is observed at a position away from the 5–7 defects. This implies that the Gauss curvature influences chemical doping near a five-membered ring (local geometry), and the mean curvature influences chemical doping at a location relatively further away from the 5–7 defects (stability of the entire model). Thus, mesoscopic bending of the graphene sheet contributed to the enhancement of chemical doping in the regions with no defects.

3.5. Synthesis and characterization of curved graphene with chemical dopants

3D curved graphenes with and without chemical dopants were synthesized by chemical vapor deposition (CVD) using NiO nanoparticles as CVD templates (Fig. S16) to obtain the similar structures suggested by the mathematical model (supplementary text). The morphology of the 3D curved graphene with and without chemical dopants was characterized by Cs-corrected scanning transmission electron microscopy (STEM). Dark-field STEM (DF-STEM) images of nitrogen and sulfur (NS) co-doped graphene, which is known as an excellent graphene catalyst [26], show curved morphologies with 100–500-nm spherical and tubular-like graphene (Fig. 4A). The corresponding selected area electron diffraction patterns of graphene show sharp diffraction spots (inset in Fig. 4A), verifying the high crystallinity of randomly orientated multi-layer graphene. A high-resolution TEM (HRTEM) image of the doped graphene lattice at the curved region reveals the topological 5–7 defects (yellow lines) with a vacancy-induced heavily disordered lattice of carbon hexagons that form the curved graphene lattice (Fig. 4B). The HRTEM image of the flat region shows a point defect induced by the chemical dopant (Fig. S17). Moreover, the DF-STEM image and the corresponding elemental mappings obtained by EELS (Fig. 4C) demonstrate the distribution of NS dopant atoms at the curved regions (brighter contrast in the white circular regions, i.e., more chemical dopants); the distribution is not observed at the flat regions (dark contrast in the white arrow regions, i.e., considerably fewer chemical dopants) regardless of the existence of carbon atoms (green contrast on the flat regions, i.e., the major component is carbon). Additionally, the curved and flat regions of the non-doped graphene are similarly characterized, and the heavily distorted lattice is not observed (Figs. S18 and S19). These observations are also supported by X-ray photoelectron spectroscopy (XPS) and Raman spectroscopy (Figs. S20–S22, Table S5 and supplementary text). Therefore, chemical dopants can be incorporated near topological defects that are geometrically required to form the curved lattice or in the vicinity of the defects at curved regions, thus providing a model system for comparison between the mathematical model and experimental results.

3.6. On-site electrochemical hydrogen evolution reaction current mapping

On-site electrochemical measurements for real-space electrochemical hydrogen evolution reaction (HER) current mapping were obtained by SECCM (Fig. 5A), which can examine both topography and the electrochemical reaction ($H^+ + e^- \rightarrow H_2$) in a 50-nm-radius nanopipette with a 0.5 M H_2SO_4 electrolyte; these were performed to link the local structural configurations with the on-site electrochemical HER activity at the sub-micrometer level. The topography

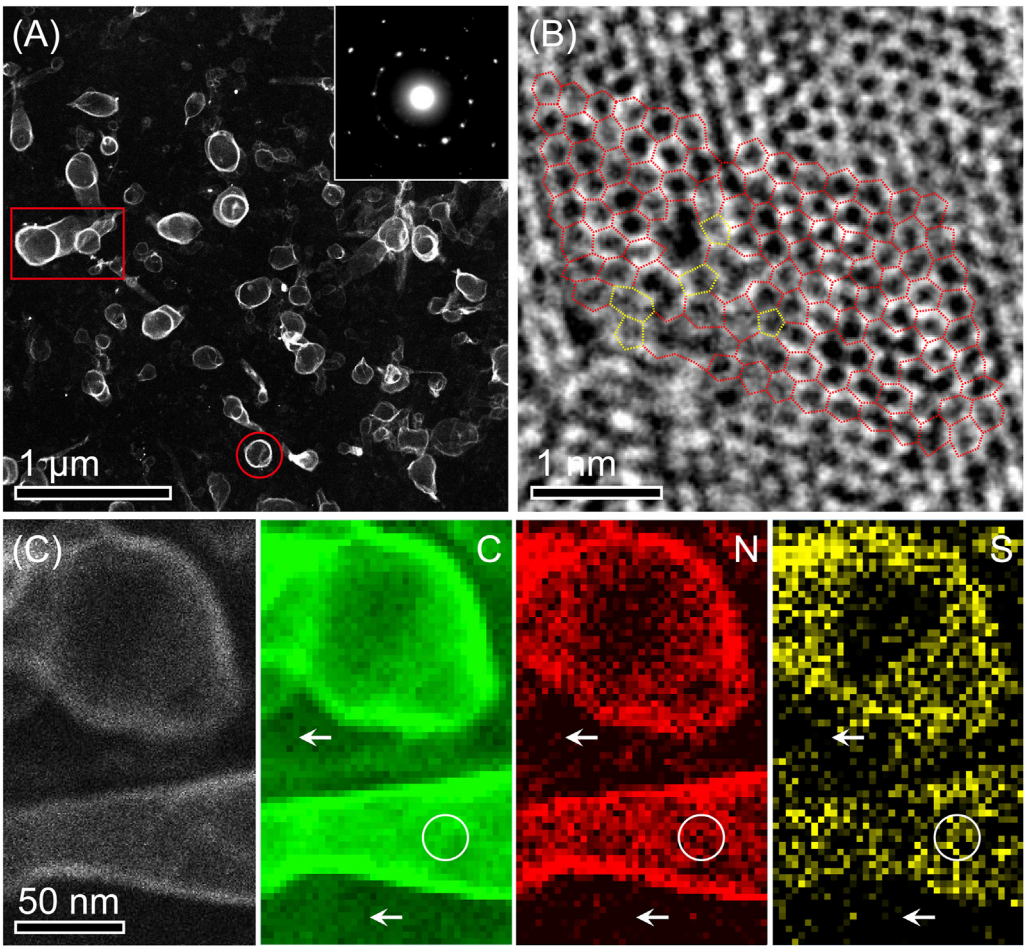

Fig. 4. Characterization of chemically doped and curved graphene. (A) DF-STEM image with a corresponding selected area electron diffraction pattern (inset). The red circle and rectangle highlight spherical and tubular-like graphene, respectively. (B) HR-TEM image of the curved parts obtained from the rectangular region in Fig. 4A. Red and yellow dotted lines indicate graphene lattices and topological defects, respectively. (C) DF-STEM image and the corresponding EELS chemical mappings of C, N, and S. White arrows and circles indicate the flat and curved graphene regions, respectively. (A colour version of this figure can be viewed online.)

and on-site HER currents for 3D curved graphenes with and without chemical dopants were simultaneously measured at −700 mV (vs. reversible hydrogen electrode (RHE)) on highly ordered pyrolytic graphite (HOPG). Notably, the large negative current accelerates hydrogen production. The mapping of the on-site reduction current on NS-doped curved graphene clearly demonstrates the dependence of the reduction currents on morphology (Fig. 5 (B and C)). Moreover, the HER line profile demonstrates topography dependent HER currents at the highly curved topographies (i.e., curved graphene) (Fig. 5 (D and E)). Conversely, the non-doped graphene demonstrates a nearly constant line profile of HER currents regardless of the curved topography (Fig. S23). To quantitatively compare the catalytic abilities of the non-doped and NS-co-doped graphene, the turnover frequency (TOF) [25,26] of hydrogen molecules was estimated using the HER current at −200 mV (vs. RHE) (Fig. S23). The TOF values of NS-co-doped graphene at the curved regions (200–900H_2/s) were approximately 100–300 times higher than those of non-doped graphene at the curved regions. This directly proves that the HER activity is affected by the morphology and morphologically induced chemical dopants at the curved regions.

4. Discussion

The potential of a simple mathematical method such as SRRI was explored as a pre-screening tool of DFT to design novel materials. Its accuracy was verified by DFT calculations, and the catalytic properties of one such material were experimentally investigated. The accuracy of the SRRI model showed a qualitative agreement with DFT calculations; moreover, its screening speed was roughly 1 billion times higher than that with DFT. The structural results obtained from both methods were used to analyze important characteristics of geometric features; they revealed that the regions on the positive Gauss curvatures induced by topological defects on the curved graphene could readily host dissimilar dopants whose differing bond lengths readjusted the structure to reduce the Gauss curvature of the graphene lattice. Moreover, vacancy defects in the heavily disordered graphene lattices (Fig. 4B) were attributed to chemical dopants, such as pyridinic nitrogen or sulfur atoms (bivalent bonds with carbons), near the topological defects for releasing the geometric frustrations, which was also consistent with the SRRI (Fig. S11) and DFT models (Figs. S10 and S11). Thus, topological defects and chemical dopants co-existed in close proximity to release geometric frustrations.

On-site electrochemical HER current mapping subsequently allowed us to reveal links between the curved geometry containing the topological defects/chemical dopants and the corresponding catalytic activity. Because conventional electrochemical measurements provided only electrochemical information averaged from entire samples, SECCM in this study showed a direct link between

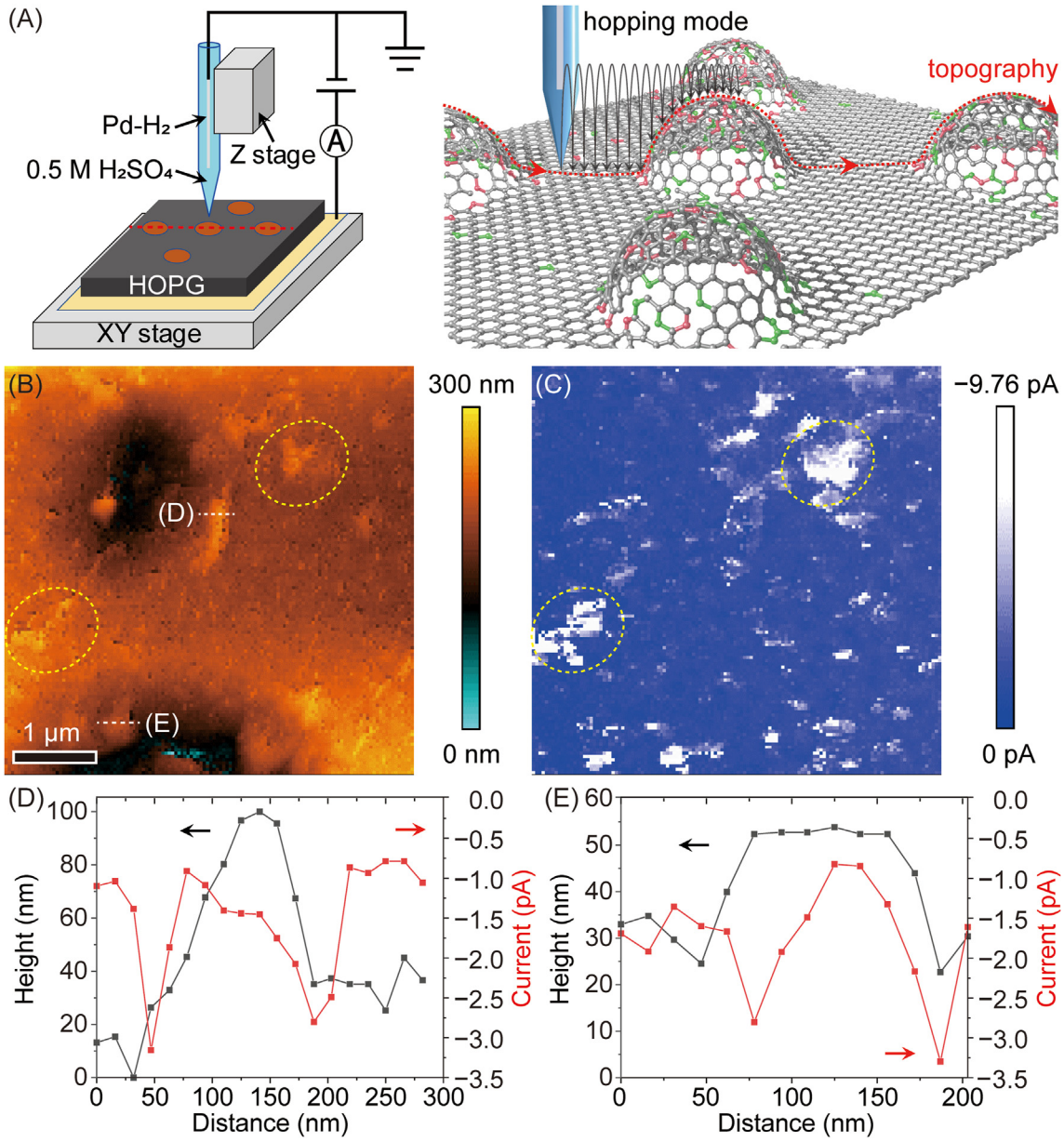

Fig. 5. SECCM HER current mapping of chemically doped curved graphene. (A) Schematic illustration of the experimental setup and a scan of the chemically doped porous graphene. Red and green spheres represent NS atoms, respectively. (B) Topography and (C) HER current mapping and (D and E) HER current line profile of NS-doped curved graphene. Yellow and white dotted lines in the topography images show the topology dependent HER current for the mapping and line profile positions, respectively. The red and black lines represent the current and height, respectively. (A colour version of this figure can be viewed online.)

the geometry and electrochemical activity. The co-existence and coadjacence of heteroatoms such as NS at the atomic level clearly resulted in preferable, catalytically active sites via synergistic effects, which were confirmed by experimental results obtained from all the samples and DFT calculations [26,50–52]. Such interactions with dopants can optimize local electronic structures, and the Gibbs free energy of H* adsorption, $|\Delta G_{H^*}|$, can be nearly zero owing to the cooperation of the dopants near the topological defect sites on the 3D curved graphene lattice [25,51]. Moreover, experimental and theoretical analyses have suggested that the enhancement of electronic density of states on graphene accelerates the local electrochemical reactions [31], and the 5–7 defects enhance the catalytic ability of chemically doped curved graphenes [25]. This indicates that the SECCM measurements can successfully detect the origin of high catalytic activity (global properties) caused by the 5–7 defects (local structures that can be described by the geometry of discrete surfaces). Thus, the curved graphene induced topological defects and enhanced the electronic density of states, which hosted the chemical dopants; the curved graphene demonstrated high catalytic activity, as demonstrated by the SECCM measurements, which suggests that SRRI can serve as a pre-screening and complementary tool of DFT to design and explore novel materials, including novel 2D materials such as boron nitride, silicene, germanene, phosphorene, and transition-metal dichalcogenides.

5. Conclusion

A new mathematical model based on the standard realization was introduced as a pre-screening and complementary tool to DFT,

and the relationship between the Gauss/mean curvatures and catalytic properties of 3D curved graphene were investigated. The mathematical model successfully captured the essence of structural changes. The accuracy of geometric features obtained via SRRI suggests its suitability for serving as a pre-screening and complementary tool for DFT in material design, as well as for cross-checking with DFT calculations. In particular, a carbon atom at regions of relatively large Gauss curvature around the atom was relatively easily replaced by a chemical dopant to release its geometric frustration, as confirmed by doping energy calculations using DFT. In addition, the curved graphene (i.e., large mean curvature) contributed chemical doping at a location relatively further away from the 5–7 defects. These enabled us to establish a link between geometry and the doping energetics to infer the properties of the material. In the experimental verification, 3D curved graphenes with a high density of geometrically required topological defects were found to accommodate several chemical dopants on the curved lattice, and exhibited higher catalytic activity on the curved regions than on the flat regions, as confirmed by on-site electrochemical measurements. Although the accuracy of standard realization does not reach that of DFT calculations, the mathematical method described herein can be an effective and universal approach for pre-screening in DFT calculations for material design. SRRI can also be used as a pre-screening tool to explore new 2D/3D carbon materials by combining with the FF/DFT model in a complementary manner.

CRediT authorship contribution statement

Andreas Dechant: Methodology, Software, Formal analysis, Data curation, Writing – original draft. **Tatsuhiko Ohto:** Methodology, Software, Formal analysis, Data curation, Writing – original draft. **Yoshikazu Ito:** Validation, Investigation, Resources, Writing – original draft, Visualization. **Marina V. Makarova:** Validation, Investigation. **Yusuke Kawabe:** Validation, Investigation. **Tatsufumi Agari:** Validation, Investigation. **Hikaru Kumai:** Validation, Investigation. **Yasufumi Takahashi:** Methodology, Software. **Hisashi Naito:** Methodology, Formal analysis, Writing – review & editing. **Motoko Kotani:** Conceptualization, Methodology, Writing – review & editing, Supervision, Project administration, Funding acquisition.

Declaration of competing interest

The authors declare that they have no known competing financial interests or personal relationships that could have appeared to influence the work reported in this paper.

Acknowledgment

We thank Ms. Kazuyo Omura at the Institute for Material Research in Tohoku University for XPS measurements. We used the supercomputer of ACCMS, Kyoto University for DFT calculations. This work was sponsored by JSPS Grant-in-Aid for Scientific Research on Innovative Areas “Discrete Geometric Analysis for Materials Design”: Grant Number JP17H06460, JP17H06465, JP17H06466, JP18H04477, JP20H04639, JP20H04628; JSPS KAKENHI Grant Number JP19K15505, JP21H02037, JP20K21141; World Premier International Research Center Initiative (WPI), MEXT, Japan; JST-PRESTO (Grant Number JPMJPR18T8); NIMS micro-structural characterization platform as a program of “Nanotechnology Platform Project,” MEXT, Japan, Grant number JPMXP09A19NM0033; a cooperative program (Proposal No. 202011-CRKEQ-0001) of the CRDAM-IMR, Tohoku University; Asahi Glass Foundation, Hokuriku Bank (Grant-in-Aid for Young Scientists), and Murata Science Foundation are all thankfully acknowledged for financial support. Andreas Dechant, Tatsuhiko Ohto contributed equally to this work.

Appendix B. Supplementary data

Supplementary data to this article can be found online at https://doi.org/10.1016/j.carbon.2021.06.004.

References

[1] A.K. Geim, K.S. Novoselov, The rise of graphene, Nat. Mater. 6 (2007) 183–191, https://doi.org/10.1038/nmat1849.
[2] K.S. Novoselov, A.K. Geim, S.V. Morozov, D. Jiang, M.I. Katsnelson, I.V. Grigorieva, S.V. Dubonos, A.A. Firsov, Two-dimensional gas of massless Dirac fermions in graphene, Nature 438 (2005) 197–200, https://doi.org/10.1038/nature04233.
[3] A.H. Castro Neto, F. Guinea, N.M.R. Peres, K.S. Novoselov, A.K. Geim, The electronic properties of graphene, Rev. Mod. Phys. 81 (1) (2009) 109–162, https://doi.org/10.1103/RevModPhys.81.109.
[4] A.K. Geim, Graphene: status and prospects, Science 324 (2009) 1530–1534, https://doi.org/10.1126/science.1158877.
[5] K.S. Novoselov, V.I. Fal'ko, L. Colombo, P.R. Gellert, M.G. Schwab, K. Kim, A roadmap for graphene, Nature 490 (2012) 192–200, https://doi.org/10.1038/nature11458.
[6] S. Park, R.S. Ruoff, Chemical methods for the production of graphenes, Nat. Nanotechnol. 4 (2009) 217–224, https://doi.org/10.1038/nnano.2009.58.
[7] Z. Sun, S. Fang, Y.H. Hu, 3D graphene materials: from understanding to design and synthesis control, Chem. Rev. 120 (2020) 10336–10453, https://doi.org/10.1021/acs.chemrev.0c00083.
[8] C. Liu, Z. Yu, D. Neff, A. Zhamu, B.Z. Jang, Graphene-based supercapacitor with an ultrahigh energy density, Nano Lett. 10 (2010) 4863–4868, https://doi.org/10.1021/nl102661q.
[9] Y. Wang, Z. Shi, Y. Huang, Y. Ma, C. Wang, M. Chen, Y. Chen, Supercapacitor devices based on graphene materials, J. Phys. Chem. C 113 (2009) 13103–13107, https://doi.org/10.1021/jp902214f.
[10] L.L. Zhang, R. Zhou, X.S. Zhao, Graphene-based materials as supercapacitor electrodes, J. Mater. Chem. 20 (2010) 5983–5992, https://doi.org/10.1039/c000417k.
[11] S. Han, D. Wu, S. Li, F. Zhang, X. Feng, Porous graphene materials for advanced electrochemical energy storage and conversion devices, Adv. Mater. 26 (2014) 849–864, https://doi.org/10.1002/adma.201303115.
[12] X.H. Xia, D.L. Chao, Y.Q. Zhang, Z.X. Shen, H.J. Fan, Three-dimensional graphene and their integrated electrodes, Nano Today 9 (2014) 785–807, https://doi.org/10.1016/j.nantod.2014.12.001.
[13] X. Huang, Z. Zeng, Z. Fan, J. Liu, H. Zhang, Graphene-based electrodes, Adv. Mater. 24 (2012) 5979–6004, https://doi.org/10.1002/adma.201201587.
[14] G. Wu, N.H. Mack, W. Gao, S. Ma, R. Zhong, J. Han, J.K. Baldwin, P. Zelenay, Nitrogen-doped graphene-rich catalysts derived from heteroatom polymers for oxygen reduction in nonaqueous lithium–O_2 battery cathodes, ACS Nano 6 (2012) 9764–9776, https://doi.org/10.1021/nn303275d.
[15] Y. Jiao, Y. Zheng, M. Jaroniec, S.Z. Qiao, Origin of the electrocatalytic oxygen reduction activity of graphene-based catalysts: a roadmap to achieve the best performance, J. Am. Chem. Soc. 136 (2014) 4394–4403, https://doi.org/10.1021/ja500432h.
[16] X. Liu, L. Dai, Carbon-based metal-free catalysts, Nat. Rev. Mater. 1 (2016) 16064, https://doi.org/10.1038/natrevmats.2016.64.
[17] J. Zhang, Z. Zhao, Z. Xia, L. Dai, A metal-free bifunctional electrocatalyst for oxygen reduction and oxygen evolution reactions, Nat. Nanotechnol. 10 (2015) 444–452, https://doi.org/10.1038/nnano.2015.48.
[18] L. Qu, Y. Liu, J.B. Baek, L. Dai, Nitrogen-doped graphene as efficient metal-free electrocatalyst for oxygen reduction in fuel cells, ACS Nano 4 (2010) 1321–1326, https://doi.org/10.1021/nn901850u.
[19] J. Liang, Y. Jiao, M. Jaroniec, S.Z. Qiao, Sulfur and nitrogen dual-doped mesoporous graphene electrocatalyst for oxygen reduction with synergistically enhanced performance, Angew. Chem. Int. Ed. 51 (2012) 11496–11500, https://doi.org/10.1002/anie.201206720.
[20] L. Lai, J.R. Potts, D. Zhan, L. Wang, C.K. Poh, C. Tang, H. Gong, Z. Shen, J. Lin, R.S. Ruoff, Exploration of the active center structure of nitrogen-doped graphene-based catalysts for oxygen reduction reaction, Energy Environ. Sci. 5 (2012) 7936–7942, https://doi.org/10.1039/c2ee21802j.
[21] Y. Ito, H.J. Qiu, T. Fujita, Y. Tanabe, K. Tanigaki, M. Chen, Bicontinuous nanoporous N-doped graphene for oxygen reduction reaction, Adv. Mater. 26 (2014) 4145–4150, https://doi.org/10.1002/adma.201400570.
[22] T. Kiryu, M. Koshino, Quantum Hall effect in three-dimensional graphene, Phys. Rev. B 99 (2019), https://doi.org/10.1103/PhysRevB.99.085443.
[23] M. Koshino, H. Aoki, Dirac electrons on three-dimensional graphitic zeolites: a scalable mass gap, Phys. Rev. B 93 (2016), https://doi.org/10.1103/PhysRevB.93.041412.
[24] Y. Tanabe, Y. Ito, K. Sugawara, M. Koshino, S. Kimura, T. Naito, I. Johnson, T. Takahashi, M. Chen, Dirac Fermion kinetics in 3D curved graphene, Adv.

Mater. 32 (2020), e2005838, https://doi.org/10.1002/adma.202005838.
[25] Y. Ito, Y. Shen, D. Hojo, Y. Itagaki, T. Fujita, L. Chen, T. Aida, Z. Tang, T. Adschiri, M. Chen, Correlation between chemical dopants and topological defects in catalytically active nanoporous graphene, Adv. Mater. 28 (2016) 10644–10651, https://doi.org/10.1002/adma.201604318.
[26] Y. Jiao, Y. Zheng, K. Davey, S.-Z. Qiao, Activity origin and catalyst design principles for electrocatalytic hydrogen evolution on heteroatom-doped graphene, Nat. Energy 1 (2016) 16130, https://doi.org/10.1038/nenergy.2016.130.
[27] M. Kotani, H. Naito, T. Omori, A discrete surface theory, Comput. Aided Geomet. Des. 58 (2017) 24–54, https://doi.org/10.1016/j.cagd.2017.09.002.
[28] M. Tagami, Y. Liang, H. Naito, Y. Kawazoe, M. Kotani, Negatively curved cubic carbon crystals with octahedral symmetry, Carbon 76 (2014) 266–274, https://doi.org/10.1016/j.carbon.2014.04.077.
[29] M. Kotani, T. Sunada, Standard realizations of crystal lattices via harmonic maps, Trans. Am. Math. Soc. 353 (2001) 1–20, https://doi.org/10.1090/S0002-9947-00-02632-5.
[30] A.G. Güell, N. Ebejer, M.E. Snowden, K. McKelvey, J.V. Macpherson, P.R. Unwin, Quantitative nanoscale visualization of heterogeneous electron transfer rates in 2D carbon nanotube networks, Proc. Natl. Acad. Sci. U.S.A. 109 (2012) 11487–11492, https://doi.org/10.1073/pnas.1203671109.
[31] A.G. Güell, A.S. Cuharuc, Y.R. Kim, G. Zhang, S.Y. Tan, N. Ebejer, P.R. Unwin, Redox-dependent spatially resolved electrochemistry at graphene and graphite step edges, ACS Nano 9 (2015) 3558–3571, https://doi.org/10.1021/acsnano.5b00550.
[32] C.H. Chen, K.E. Meadows, A. Cuharuc, S.C.S. Lai, P.R. Unwin, High resolution mapping of oxygen reduction reaction kinetics at polycrystalline platinum electrodes, Phys. Chem. Chem. Phys. 16 (2014) 18545–18552, https://doi.org/10.1039/c4cp01511h.
[33] C.L. Bentley, M. Kang, F.M. Maddar, F. Li, M. Walker, J. Zhang, P.R. Unwin, Electrochemical maps and movies of the hydrogen evolution reaction on natural crystals of molybdenite (MoS_2): basal vs. edge plane activity, Chem. Sci. 8 (2017) 6583–6593, https://doi.org/10.1039/c7sc02545a.
[34] Y. Takahashi, A. Kumatani, H. Munakata, H. Inomata, K. Ito, K. Ino, H. Shiku, P.R. Unwin, Y.E. Korchev, K. Kanamura, T. Matsue, Nanoscale visualization of redox activity at lithium-ion battery cathodes, Nat. Commun. 5 (2014) 5450, https://doi.org/10.1038/ncomms6450.
[35] Y. Takahashi, T. Yamashita, D. Takamatsu, A. Kumatani, T. Fukuma, Nanoscale kinetic imaging of lithium ion secondary battery materials using scanning electrochemical cell microscopy, Chem. Commun. 56 (2020) 9324–9327, https://doi.org/10.1039/d0cc02865g.
[36] G. Kresse, J. Hafner, Norm-conserving and ultrasoft pseudopotentials for first-row and transition elements, J. Phys. Condens. Matter 6 (1994) 8245–8257, https://doi.org/10.1088/0953-8984/6/40/015.
[37] P.E. Blöchl, Projector augmented-wave method, Phys. Rev. B 50 (1994) 17953–17979, https://doi.org/10.1103/physrevb.50.17953.
[38] J.P. Perdew, K. Burke, M. Ernzerhof, Generalized gradient approximation made simple, Phys. Rev. Lett. 77 (1996) 3865–3868, https://doi.org/10.1103/PhysRevLett.77.3865.
[39] Y. Ito, M. Izumi, D. Hojo, M. Wakisaka, T. Aida, T. Adschiri, One-step nanoporous structure formation using NiO nanoparticles: pore size control and pore size dependence of hydrogen evolution reaction, Chem. Lett. 46 (2017) 267–270, https://doi.org/10.1246/cl.161017.
[40] Y. Takahashi, Y. Kobayashi, Z. Wang, Y. Ito, M. Ota, H. Ida, A. Kumatani, K. Miyazawa, T. Fujita, H. Shiku, Y.E. Korchev, Y. Miyata, T. Fukuma, M. Chen, T. Matsue, High-resolution electrochemical mapping of the hydrogen evolution reaction on transition-metal dichalcogenide nanosheets, Angew. Chem. Int. Ed. 59 (2020) 3601–3608, https://doi.org/10.1002/anie.201912863.
[41] C.H. Chen, L. Jacobse, K. McKelvey, S.C.S. Lai, M.T.M. Koper, P.R. Unwin, Voltammetric scanning electrochemical cell microscopy: dynamic imaging of hydrazine electro-oxidation on platinum electrodes, Anal. Chem. 87 (2015) 5782–5789, https://doi.org/10.1021/acs.analchem.5b00988.
[42] W.L. Jorgensen, D.S. Maxwell, J. Tirado-Rives, Development and testing of the OPLS All-Atom force field on conformational energetics and properties of organic liquids, J. Am. Chem. Soc. 118 (1996) 11225–11236, https://doi.org/10.1021/ja9621760.
[43] M. Kotani, H. Naito, C. Tao, Construction of continuum from a discrete surface by its iterated subdivisions, to appear, Tohoku Math. J., 2021 arXiv:1806.03531.
[44] T. Sunada, Topological Crystallography, Springer, Japan, Tokyo, 2013.
[45] D. Cvetković, T. Rowlinson, S. Simić, An Introduction to the Theory of Graph Spectra, Cambridge University Press, Cambridge, 2010.
[46] J. Lahiri, Y. Lin, P. Bozkurt, I.I. Oleynik, M. Batzill, An extended defect in graphene as a metallic wire, Nat. Nanotechnol. 5 (2010) 326–329, https://doi.org/10.1038/nnano.2010.53.
[47] H. Terrones, M. Terrones, E. Hernández, N. Grobert, J.-C. Charlier, P.M. Ajayan, New metallic allotropes of planar and tubular carbon, Phys. Rev. Lett. 84 (2000) 1716, https://doi.org/10.1103/PhysRevLett.84.1716.
[48] M. Tagami, Y. Liang, Y. Kawazoe, M. Kotani, New growth mechanism of cubic Rh clusters composed of 8–12 atoms found by the method of Euclidean designs, Mater. Trans. 53 (2012) 459–462, https://doi.org/10.2320/matertrans.N-M2011859.
[49] A. Mizuno, Y. Shuku, M.M. Matsushita, M. Tsuchiizu, Y. Hara, N. Wada, Y. Shimizu, K. Awaga, 3D spin-liquid state in an organic hyperkagome lattice of mott dimers, Phys. Rev. Lett. 119 (2017), 057201, https://doi.org/10.1103/PhysRevLett.119.057201.
[50] J. Duan, S. Chen, M. Jaroniec, S.Z. Qiao, Heteroatom-doped graphene-based materials for energy-relevant electrocatalytic processes, ACS Catal. 5 (2015) 5207–5234, https://doi.org/10.1021/acscatal.5b00991.
[51] H. Jin, C. Guo, X. Liu, J. Liu, A. Vasileff, Y. Jiao, Y. Zheng, S.Z. Qiao, Emerging two-dimensional nanomaterials for electrocatalysis, Chem. Rev. 118 (2018) 6337–6408, https://doi.org/10.1021/acs.chemrev.7b00689.
[52] Y. Ito, C. Weitao, T. Fujita, Z. Tang, M. Chen, High catalytic activity of nitrogen and sulfur co-doped nanoporous graphene in the hydrogen evolution reaction, Angew. Chem. Int. Ed. 54 (2015) 2131–2136, https://doi.org/10.1002/anie.201410050.